

## Stresses in the Lunar Interior: Insights From Slip Directions in the A01 Deep Moonquake Nest

A. R. Turner<sup>1</sup> , J. C. Hawthorne<sup>1</sup> , and M. Gaddes<sup>2</sup> 

<sup>1</sup>Department of Earth Sciences, University of Oxford, Oxford, UK, <sup>2</sup>COMET, University of Leeds, Leeds, UK

### Key Points:

- We examine why some moonquakes appear to slip in the opposite direction from the others
- Using moonquake waveforms, we infer that slip direction changes through time because of tidal loading
- The results indicate that the tidal stress, with magnitude 0.1 MPa, is larger than the tectonic stress

### Supporting Information:

Supporting Information may be found in the online version of this article.

### Correspondence to:

A. R. Turner,  
[alice.turner@earth.ox.ac.uk](mailto:alice.turner@earth.ox.ac.uk)

### Citation:

Turner, A. R., Hawthorne, J. C., & Gaddes, M. (2022). Stresses in the lunar interior: Insights from slip directions in the A01 deep moonquake nest. *Journal of Geophysical Research: Planets*, 127, e2022JE007364. <https://doi.org/10.1029/2022JE007364>

Received 3 MAY 2022  
Accepted 21 NOV 2022

**Abstract** We probe the present-day stresses in the lunar interior by examining the slip directions of moonquakes in the A01 nest. In this nest, some deep moonquakes appear to slip “backwards,” in the opposite direction to other events. We assess whether these changes in slip direction result from a spatial variation in the tectonic stress or from a temporal variation in the tidal stress. To test these two options, we first show that a dominant tectonic stress implies deep moonquakes can only slip in one direction: forwards and backwards, while a dominant tidal stress could allow moonquakes to slip in more directions: any combination of forwards, backwards, left, and right. Then we look for the number of slip directions; we separate the deep moonquake waveforms into slip directions using a principal component analysis technique. We find two slip directions present in the A01 deep moonquake nest. The moonquakes slip in a variety of directions as time evolves. This observation implies that the tidal stresses drive deep moonquakes. Additionally, these results place a new constraint on the magnitude of the tectonic stresses at depth; they must be smaller than the modeled tidal stress of ~0.1 MPa.

**Plain Language Summary** The stresses that act in the lunar interior are not well known but are important for improving our knowledge of the interior of the Moon and its evolution. Deep inside the Moon, at depths between 700 and 1,200 km, moonquakes occur approximately every 27 days, suggesting they are influenced by Earth's time-varying gravitational pull: by Earth-induced tides. Are the tides responsible for generating deep moonquakes? Or is long-term tectonic stress, in addition to the tidal stresses responsible? Using the waveforms of these deep moonquakes, we aim to determine the relative magnitudes of the tidal and tectonic stresses acting deep in the lunar interior. To do this, we look at the directions in which the moonquakes slip. We observe that deep moonquakes slip in a variety of different directions, which can only be caused by tidal stresses. Since these deep moonquakes are generated by the tides, this observation reveals that tectonic stresses in the lunar interior must be smaller than 0.1 MPa.

## 1. Introduction

During the Apollo missions in the 1970s, four seismic stations were placed on the Moon's near side. These seismic stations recorded hundreds of deep moonquakes, which occur at depths of 700–1,200 km.

Deep moonquakes tend to occur in clusters called “nests.” In each nest, moonquakes occur at monthly intervals; they are seemingly influenced by the Earth-induced tidal stresses (Lammlein, 1977; Minshall & Goulet, 1988; Nakamura, 1978; Toksöz et al., 1977; Weber et al., 2009, 2010). However, the details of that influence remain unclear. Do tides trigger deep moonquakes by adding a small perturbation in stress on top of a large long-term tectonic stress? Or do tides generate deep moonquakes by providing most or all the stress at depth? In this study, we aim to constrain the relative magnitudes of tidal and tectonic stresses and their role in generating deep moonquakes. To do so, we theorize that if tectonic stress is dominant, a moonquake fault will always slip in one direction, while if the tidal stress is dominant, the fault can slip in a variety of directions. We use deep moonquake waveforms to determine the number of slip directions.

Previously, there have been two approaches to understanding the relationship between deep moonquakes and tidal stress: tidal modeling (e.g., Araki, 2001; Cheng & Toksöz, 1978; Toksöz et al., 1977; Weber et al., 2010) and seismological observations (e.g., Kawamura et al., 2017; Koyama & Nakamura, 1980; Nakamura, 1978; Weber et al., 2010). Some of these studies suggest that tidal stresses dominate the stress field in the deep moonquake source region. The tidal stress is large enough to account for the entire stress released in deep moonquakes (Kawamura et al., 2017). And large tidal stresses could also explain why some moonquakes appear to slip “backwards”: in the opposite directions of most moonquakes in the nest. Moonquake slip directions could reverse if

the tidal stresses dominate the local stress field and allow a reversal in the stress direction over their monthly oscillations (Nakamura, 1978; Toksöz et al., 1977).

However, other observations suggest that tectonic stresses dominate the local stress field. The tidal stresses may be larger than moonquake stress release, but local confining stresses are 10,000 times larger still (Minshull & Goulety, 1988). Additionally, studies that resolve the tangential tidal stress and stress rates onto candidate fault planes (described by a strike and dip) find that deep moonquakes do not always occur when the tangential tidal stress is the highest (Araki, 2001; Weber et al., 2009), suggesting that deep moonquakes must respond to some non-tidal stress.

### 1.1. Motivation to Understand the Relative Magnitudes of the Tidal and Tectonic Stresses

We were motivated to understand the relative magnitudes of the tidal and tectonic stresses for two reasons: (a) to provide observational constraints of the stresses in the lunar interior and (b) to understand the mechanism of deep moonquakes.

#### 1.1.1. Insights for the Lunar Interior

If tectonic stresses dominate the local stress field, they could have a variety of origins. They could be elastic stresses preserved from early lunar events (Weber et al., 2009); stresses generated by continuing weak convection (Frohlich & Nakamura, 2009); thermal stress from contraction of the lunar interior as it cools (Minshull & Goulety, 1988; Solomon & Chaiken, 1976); volumetric stresses from phase changes (Weber et al., 2009); or stresses concentrated around compositional heterogeneities within the lunar interior (Qin et al., 2012; Sakamaki et al., 2010; Steinberger et al., 2015; Zhao et al., 2012). There are, however, few observational constraints on the stresses involved in these processes (Solomon & Chaiken, 1976). We may better constrain the long term stress magnitudes by understanding the stresses that drive deep moonquakes.

#### 1.1.2. Deep Moonquake Mechanisms

Understanding the stresses in the lunar interior may also help us understand deep moonquakes themselves. These ruptures are enigmatic; they are thought to occur at pressures of  $\sim 3\text{--}4$  GPa and temperatures of  $\sim 1,100\text{--}1,600^\circ\text{C}$  (e.g., Frohlich & Nakamura, 2009; Gagnepain-Beyneix et al., 2006; Garcia et al., 2019; Kawamura et al., 2017; Khan et al., 2014), where rocks are expected to deform slowly and ductilely, not in abrupt brittle failures.

Three mechanisms are commonly proposed to explain the existence of deep moonquakes: the same mechanisms proposed to generate intermediate-depth ( $\sim 100$  km) and deep ( $>410$  km) earthquakes. Deep moonquakes may occur via (a) increased pore fluid pressure, which decreases the effective normal stress and allows for brittle failure at greater depths (e.g., Brantut et al., 2011; Davies, 1999; Dobson et al., 2002; Hacker et al., 2003; Meade & Jeanloz, 1991; Proctor & Hirth, 2015). Alternatively, they may occur via (b) thermal runaway, where a large initial shear stress and a small increase in strain rate lead to heating, runaway weakening, and failure (e.g., John et al., 2009; Karato et al., 2001; Kelemen & Hirth, 2007; Ogawa, 1987; Thielmann, 2018; Thielmann et al., 2015). Or finally, moonquakes may occur via (c) a volume change and faulting associated with a mineralogical phase change (e.g., Burnley et al., 1991; Green & Burnley, 1989; Kirby, 1987; Kirby et al., 1996; Schubnel et al., 2013).

### 1.2. Reversed Polarity Moonquakes

In our search for the relative magnitudes of the tidal and tectonic stresses in the moonquake source region, we will focus on the stresses that allow reversed polarity moonquakes. Reversed polarity moonquakes generate waveforms similar to the waveforms of normal-polarity moonquakes, just flipped (Figure 1a). These reversed polarity waveforms were observed at the A01 deep moonquake nest in 1972, 1973, and 1974, interspersed with normal polarity waveforms (Frohlich & Nakamura, 2009; Koyama & Nakamura, 1980; Nakamura, 1978). They originate from the same location as the normal polarity moonquakes but imply that some moonquakes in this location slip in the opposite direction to the rest. We test two models to explain this slip reversal.

#### 1.2.1. Tectonic Plug Model

In the first proposed model, the long-term tectonic stress is larger than the oscillatory tidal stress. The shear stress at a given location is thus always in the same direction (arrows in Figure 1b). However, the stress may vary in space. Slip may occur on two parallel shear zones on either side of a moving plug, as sometimes observed during

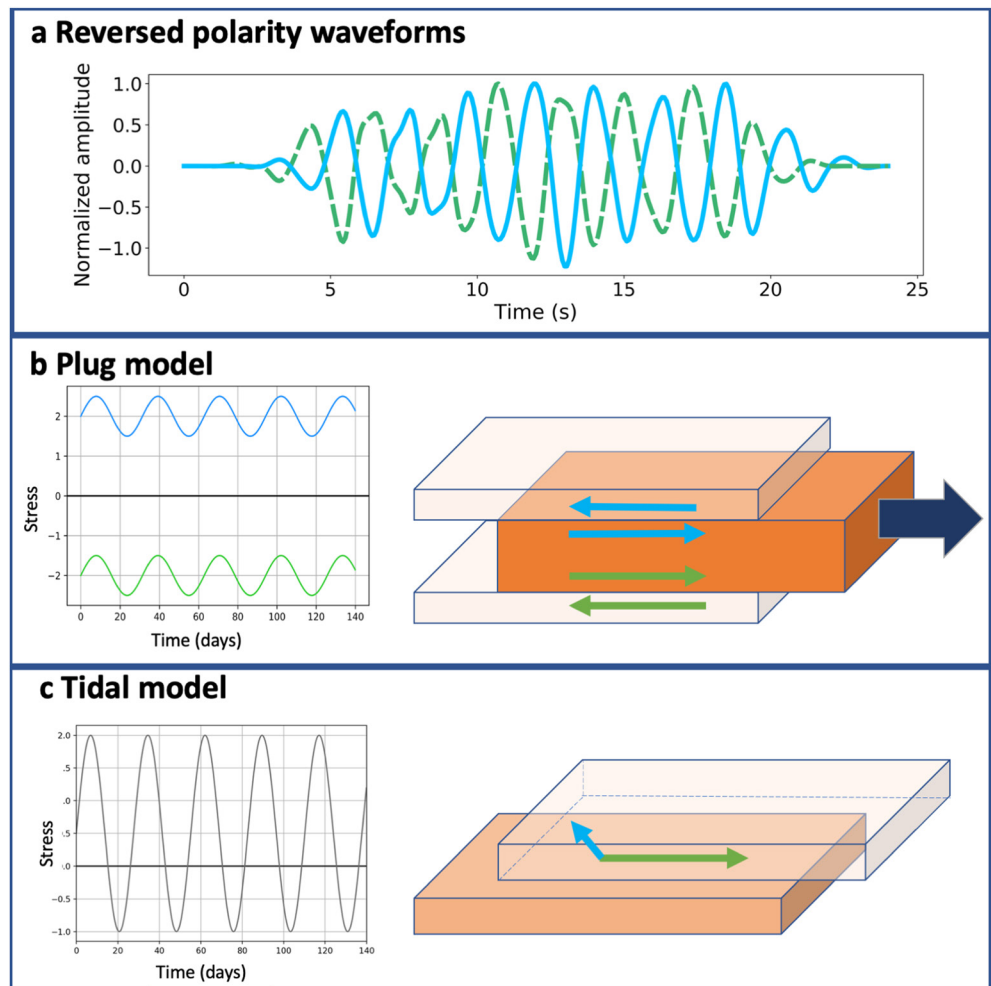


**Figure 1.** (a) A pair of moonquakes with reversed polarities, recorded on the east channel of station S16. The blue waveform was recorded on 17th November 1973, and the green waveform was recorded on 5th October 1975. The pair of events have a maximum cross-correlation value of  $-0.87$  in a 20-s window around the first arrival. For plotting, the windowed waveforms are band-pass filtered between 0.25 and 1.1 Hz and convolved with a 50% cosine taper. Two models have been proposed to explain the reversed polarity waveforms. In (b) the plug model, the long-term tectonic stress is larger than the oscillatory tidal stress. The stress directions (arrows) are constant in time but change from one side of the plug to the other. In (c) the tidal model, the tidal stress is larger than the tectonic stress. Slip occurs on a single fault plane, and the stress direction (arrows) changes over time, assuming a range of rakes.

volcanic dyke intrusions (White et al., 2011). This model is similar to the secular stress model presented by Weber et al. (2010), but with an explicit explanation for the reversal of slip: the motion of the plug would produce moonquakes that slip in roughly opposite directions, as observed.

### 1.2.2. Tidal Model

In the second proposed model, first suggested by Nakamura (1978) and more recently by Weber et al. (2010), the oscillatory tidal stress is larger than the long-term tectonic stress. The stress direction can thus vary with time on a fixed fault plane (Figure 1c). Reversed polarity moonquakes can occur on the same fault plane as normal moonquakes.

### 1.3. Our Approach: Differentiating Between Models for Apparent Slip Reversal in the A01 Nest

To test these models, we note that in the plug model, the stress is either forwards or backwards; there is one stress direction for each side of the plug. But in the tidal model, the stress can also rotate to different rakes along the fault plane (from the green to the blue arrow in Figure 1c). Since faults slip in the direction of the stress, we can

make a similar statement about moonquake slip directions. In the plug model, moonquakes can slip forwards and backwards, but in the tidal model, moonquakes can slip in 2-D space, with any combination of left, right, forwards, and backwards.

We aim to determine whether the normal and reversed polarity moonquakes in the A01 nest slip along one direction (forwards and backwards) or along two directions (left, right, forwards, and backwards). Equivalently, we aim to determine if deep moonquakes occur on a fixed fault plane with two fixed rakes (forwards and backwards) or on a fixed fault plane with a time-varying rake. To do so, we will separate the energy in the deep moonquake waveforms into principal components, which we then interpret as one or more slip directions. We will apply a range of statistical tests to assess the slip directions' robustness.

## 2. Data Selection and Initial Processing

In this study, we focus on the A01 deep moonquake nest. The nest is located 18° southwest of station S12 at a depth of 870 km (Nakamura, 2005) and is the most active moonquake nest, providing enough good quality data to determine the number of slip directions.

We download the 3-component long period Apollo seismic data from the GEOSCOPE observatory through the Institut de Physique du Globe de Paris (IPGP) data center (<http://datacenter.ipgp.fr/>). The original data were stored on magnetic tape, but it has been extracted from binary to Standard for the Exchange of Earthquake Data format for easier access (Nunn, Weber, & Panning, 2020; Nunn et al., 2017). The data were recorded in two instrument response modes, flat and peaked mode. The peaked instrument response mode was the natural response of the seismometer, with a peak in the frequency response at about 0.45 Hz (Nunn, Garcia, et al., 2020). The flat instrument mode was designed to be sensitive to a broader frequency range, from about 0.1 to 1 Hz (Nunn, Garcia, et al., 2020). We consider moonquakes recorded in the two instrumental modes and at each station separately, so we leave the data as they were recorded and do not deconvolve the instrument response. When we use the uncorrected data in peaked and flat modes, they represent the convolution of the data with the two different frequency responses of the instruments. Each of the modes enhances different frequency bands while diminishing others. The signal-to-noise ratio can vary with frequency, creating differences between the two data sets. The different signal-to-noise ratios can be observed in the plotted waveforms (illustrated in Figures S2–S8 in Supporting Information S1), where the noise amplitude in the peaked mode is lower than in the flat mode. By treating each component and instrument response mode separately, we avoid some of the issues that persist in the lunar data, such as different gains or frequency responses on different components (Nunn, Weber, & Panning, 2020).

To identify A01 moonquakes, we use the Nakamura (2003) catalog with updates from Bulow et al. (2005). Each A01 moonquake recorded at station S12 is correlated with a template event for each operational mode in a 5-min window around the first arrival (template events are given in Table S1 in Supporting Information S1 and plotted in Figure S1 in Supporting Information S1). The template was chosen as an A01 event with a high amplitude and no data gaps recorded at station S12 in each operational mode. Events will be used for the Principal component analysis (PCA) if they have a maximum cross-correlation value of greater than 0.3 with the template event in the cross-correlation window. The time shift of the maximum cross-correlation is also taken as the initial time shift to align the events. Finally, we check the events by eye to ensure no events with large data gaps or spikes in the time period of the first arrival. The same set of events is used on station S16. Events recorded at Stations 12 and 16 are rotated to the correct orientations given by Nunn, Garcia, et al. (2020), as they were misaligned when they were installed. In principle, the rotation should have minimal effect on our analysis as we are concerned with the number of slip directions, not the absolute direction of motion. The rotated A01 event waveforms are despiked using a median filter (Bulow et al., 2005), resampled to twice the original sampling rate, and band-pass filtered between 0.25 and 1.75 Hz.

We found few good quality moonquakes with clear arrivals at stations S14 or S15 and therefore analyze data from stations S12 and S16 only. After preprocessing, we have a data set of waveforms at each component, station, and instrument response. We consider 14 moonquakes recorded at station S12 on the north channel (MHN) in the peaked operation mode (Figure 2). We consider between 12 and 28 waveforms recorded on each of the east channels (MHE), in flat mode, and at station S16 (illustrated in Figures S2–S8 in Supporting Information S1). The reversed polarity waveforms recorded in each instrument mode are listed in Table S2 in Supporting Information S1. In the data recorded at station S16 in the peaked mode there are five reversed polarity events, and in the

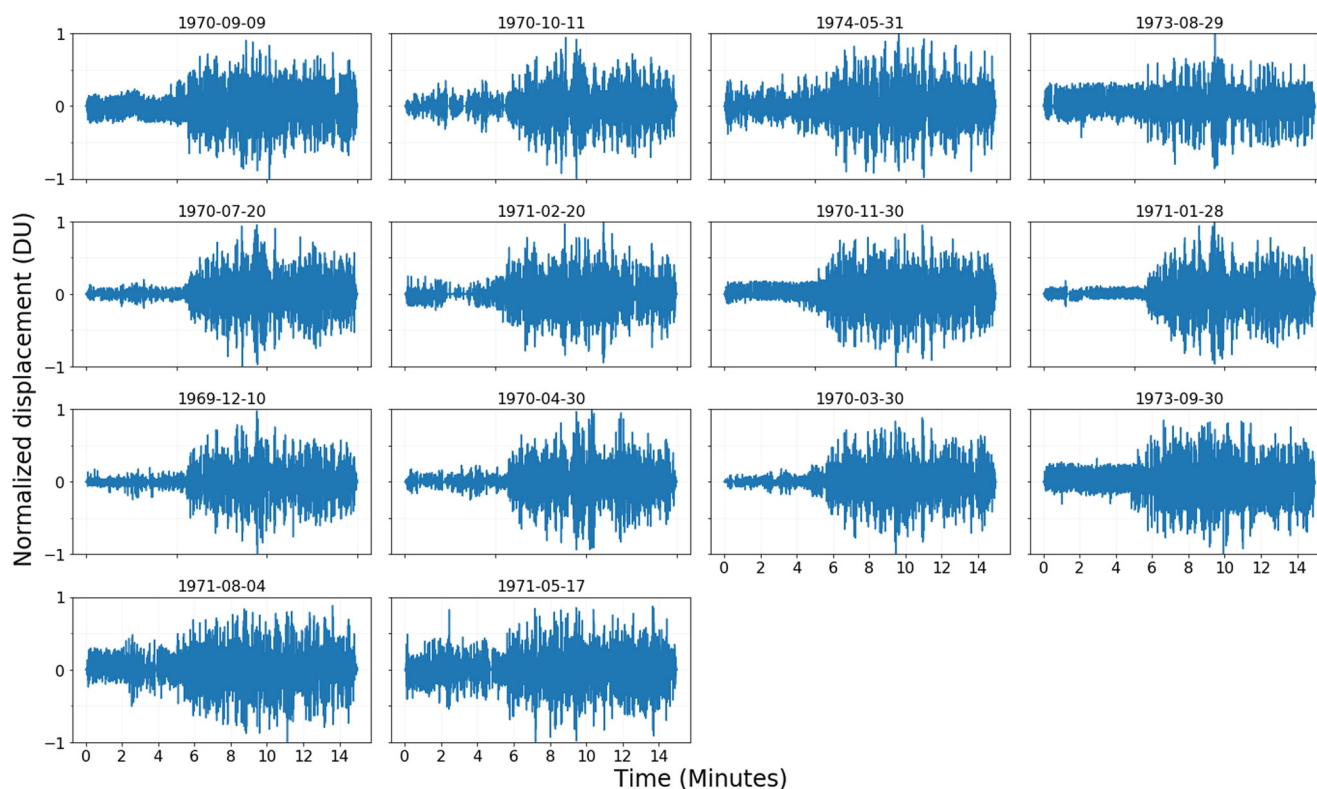


**Figure 2.** Deep moonquake waveforms used for Principal component analysis decomposition, recorded at station S12, channel MHN, in the peaked operation mode.

data recorded at station S12 in the peaked mode there are three. Due to the time the instrument was operating in flat mode, we do not identify any reversed polarity events in these subsets of the data. Nevertheless, we apply the same analysis to understand how the slip directions may vary.

### 3. Principal Component Analysis of A01 Moonquake Waveforms

To assess the stress state in the deep moonquake generating region, we examine moonquake slip directions. For terrestrial problems, researchers often determine individual earthquake's focal mechanisms—their fault planes and slip directions—using the polarities of first arrivals recorded at a number of stations (e.g., Hardebeck & Shearer, 2002; Yang et al., 2012). Some previous studies have attempted to determine a moonquake fault plane for the A01 nest (described by a strike and dip) but were unsuccessful (Araki, 2001; Weber et al., 2009). However, moonquake slip directions are not routinely estimated; it remains challenging as moonquake seismograms have emergent onsets, as shown in Figure 2 and are recorded at only four stations (Nakamura, 1978; Weber et al., 2009).

Instead, then, we determine the range of moonquake slip directions by comparing waveforms of various events in the A01 nest using PCA. PCA is a statistical method that models a set of observations as a linear combination of particular basis functions: a set of linearly uncorrelated vectors called principal components. These principal components are chosen so that the first component accommodates as much of the observed signals as possible. The second component then reconstructs as much of the remaining signal as possible, and so on until the last component accommodates only a small fraction of the signal (Bishop & Nasrabadi, 2006). PCA has previously been applied to problems in earthquake seismology. It has been used to identify dominant trends in earthquake locations (Ocaña et al., 2008), to identify similarities in recovered moment rate functions (Vasco, 1989, 1990), and to determine moment tensors of earthquakes (Vavryčuk et al., 2017).



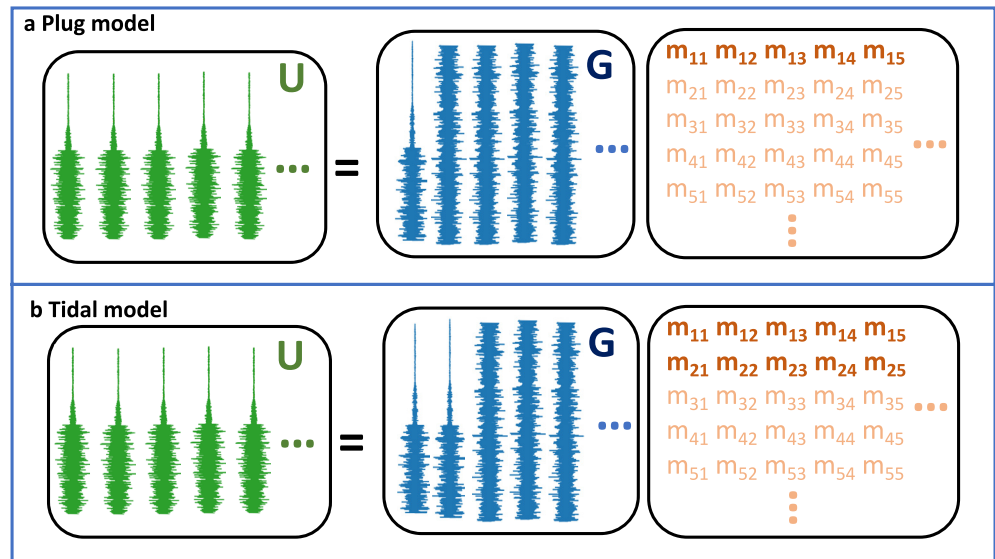


**Figure 3.** Illustration of the Principal component analysis decomposition for the A01 moonquakes. A matrix of waveforms (green, **U**) is decomposed into the principal components (blue, **G**) and the coefficients (orange, **m**). We then interpret the principal components as slip directions. (a) For the plug model, events only slip either backwards or forwards. We expect one recovered principal component to be a real Green's function of the slip direction: one principal component will contain signal and all others will contain noise. The slip coefficients  $m_{k1}$ , will be large (shown in a darker bold orange), while all others will be small. (b) For the tidal model, events can slip in any combination of left, right, backwards, and forwards. We expect two principal components to represent real Green's functions of slip: two principal components will contain signal and all others will contain noise. The slip coefficients  $m_{k1}$  and  $m_{k2}$  will be large and all others will be small.

Let us consider all the A01 moonquake seismograms  $U_k(t)$  recorded on a single channel at a single station. Since the moonquakes in a nest occur within a compact cluster only a few km wide (Nakamura, 1978), we can model the displacement at the lunar surface created by the moonquake using a moment tensor representation as follows:

$$U_k(t) = \sum_{j=1}^J G_j(t) m_{kj}. \quad (1)$$

As illustrated in Figure 3,  $U_k$  is the waveform for event  $k$ , and  $G_j$  is the Green's function: the surface displacement produced by unit moment (slip times area times local shear modulus) applied in direction  $j$  on the fault. We assume that the moonquakes all occur on the same fault, so the fault orientation (strike and dip) is constant, which leaves two directions in which the moment can be applied in  $J = 1$  or  $J = 2$ . We call  $m_{kj}$  the slip coefficient: it is the moment in direction  $j$  for event  $k$ .

If we collect the  $J$  waveforms  $U_k(t)$  observed from several A01 moonquakes  $k$  into the columns of the matrix **U**, we may note that Equation 1 has the same form as that used in the PCA: **U** = **Gm**. PCA decomposes the data matrix (**U**) into a set of coefficients (rows of **m**) multiplied by a set of basis vectors or principal components (columns of **G**). It would thus seem that we can use a PCA decomposition to recover the slip coefficients (**m**) and Green's functions (**G**) from the deep moonquake waveforms. Both **G** and **m** are unknowns but can be recovered together using PCA by also assuming the Green's functions (**G**) are uncorrelated, ordered by the variance they explain, and that each principal component explains as much of the variance of the data as possible.

However, it is important to note that the PCA decomposition always recovers the same number of principal components as waveforms (i.e., in Equation 1,  $J$  = number of events). The components are chosen such that the first components accommodate as much of the signal in the data vectors  $U_k$  as possible. Later components accommodate progressively less signal. We then interpret the principal components as the Green's functions for one or more slip directions. We expect the first few principal components to be Green's functions for the slip in one or more directions, as they can accommodate signal from multiple moonquakes. Later principal components are likely to be noise, which differs from event to event. Our challenge will be to determine which principal components represent Green's functions and which principal components represent noise (Figure 3).

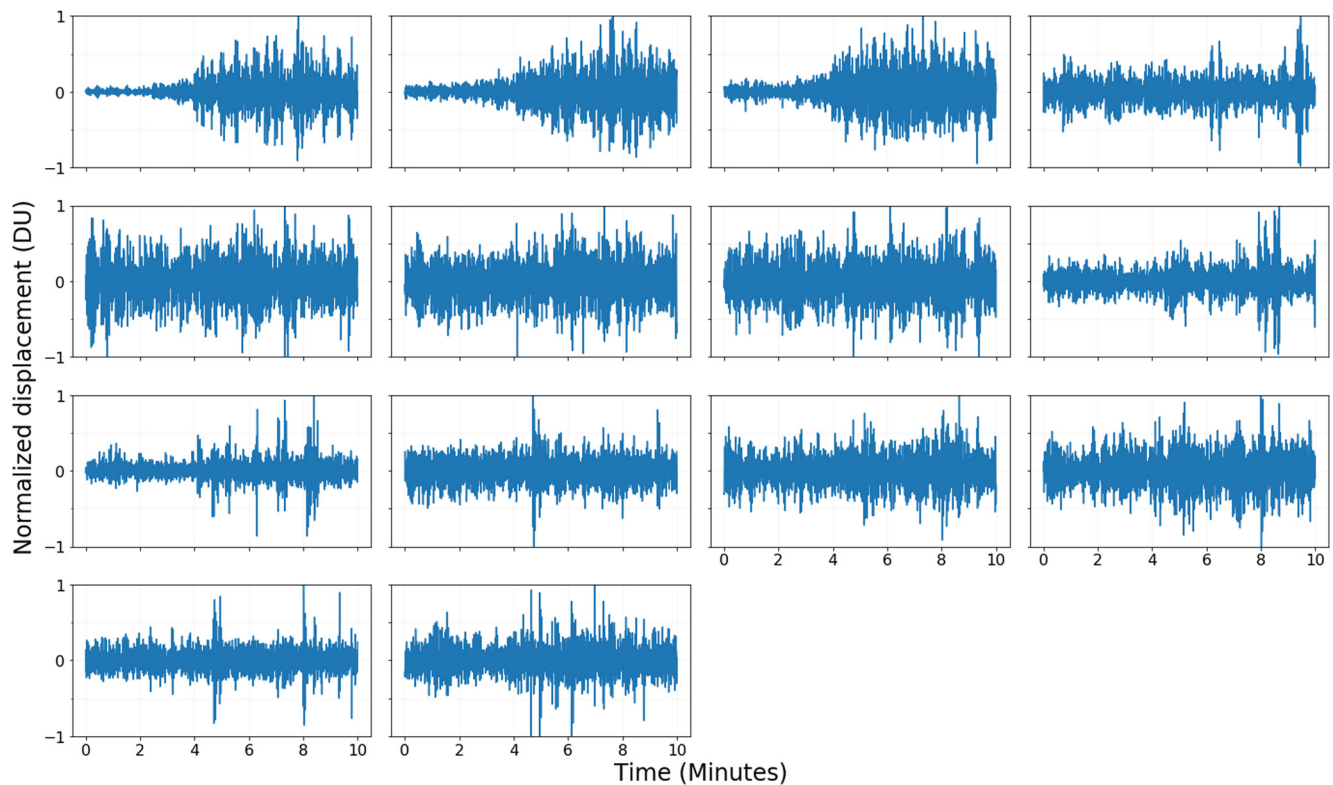


**Figure 4.** Principal components derived from the S12 MHN data in the peaked operational mode of the instrument.

The number of principal components representing Green's functions will let us distinguish between the two models of moonquake slip presented in Section 1.1. For the plug model, we hypothesize that there is a single slip direction; one principal component should have a large  $m_{k1}$  and contain signal common to multiple moonquakes, representing a real Green's function of that slip direction while all other  $m_{kj}$  should be close to zero. In contrast, the tidal model predicts two slip directions; two principal components should have two large  $m_{k1}$  and  $m_{k2}$ , representing real Green's functions of the two slip directions, and all other  $m_{kj}$  should be close to zero (Figure 3).

In carrying out the PCA, we must ensure good waveform alignment. The signal in each principal component is sensitive to waveform alignment, as time-shifted traces can be mapped into different components. Before we compute the PCA decomposition, we cross-correlate each waveform with a high-quality template event to obtain a best-fitting initial time shift, as described in Section 2. Then we apply the PCA to a 10-min window of the A01 deep moonquake waveforms, which includes the direct P and S arrivals and scattered arrivals in the coda. Finally, we fine-tune the alignment. Our bootstrap analysis suggests that events are initially aligned using cross-correlation within two or three samples, so we ensure the best alignment between the waveforms by searching 0.7 s (10 samples) around the cross-correlation time shifts to maximize the energy in the first component of the PCA.

The principal components determined from the PCA decomposition are plotted in Figure 4. We discuss their qualitative characters in Section 4. In Section 5, we examine the coefficients and principal components determined from the PCA more quantitatively.

#### 4. Qualitative Analysis of the Principal Components (G)

In our first preliminary analysis, we look at the shape of the recovered principal components. Figure 4 shows the 14 principal components for the peaked mode MHN records at station S12, ordered by the percentage of the data variance they explain. The first three principal components, which explain the most variance, have clear onsets in signal followed by decays. They have “moonquake-like” shapes, similar to the waveforms in Figure 2. These shapes suggest that the first three principal components could represent real Green's functions. Later

principal components, which explain progressively less of the variance, do not have clear onsets or decaying “moonquake-like” shapes.

Using the MHE records at station S12 (Figure S9 in Supporting Information S1), we also observe three moonquake-shaped principal components. However, when we analyze the flat mode MHN and MHE data (Figures S10 and S11 in Supporting Information S1), there are only two “moonquake-shaped” principal components.

When we analyze the waveforms recorded at station S16 (Figures S12–S15 in Supporting Information S1), we again observe three moonquake-shaped components in the decomposition of the peaked mode data and two moonquake-shaped components in the flat mode data. Our simple preliminary analysis suggests that there could be two or three principal components that contain signals common to many moonquakes and thus may represent the Green's functions of slip directions. But some of the “moonquake-like” signals may just be signal from just one moonquake, not the signal common to many moonquakes. We now wish to more robustly discriminate between those components which contain signal and those which are just noise.

## 5. Quantitative Analysis of the Number of Principal Components

Next, we aim to more rigorously determine whether each derived principal component represents a Green's function or represents noise. We quantitatively analyze the “slip” coefficients  $m$  obtained for each principal component and event (Section 5.1) as well as the principal component vectors  $G$  themselves (Section 5.2).

### 5.1. Analyzing the Unbiased Principal Component Coefficients ( $m'$ )

The PCA coefficients  $m_{kj}$  determine how much of each principal component  $j$  is needed to reconstruct the seismogram generated by moonquake  $k$ . If a principal component  $G_j(t)$  represents a real Green's function, its coefficients are likely to be large for multiple moonquakes  $k$ . We therefore aim to assess the coefficients' values.

To accurately assess the coefficients' values, we need to compare the principal component vectors with “unseen” validation waveforms. We want to know how well each principal component can be used to reconstruct moonquake waveforms that were not employed in creating the principal component vectors.

To achieve this, we use a method similar to “leave-one-out cross-validation” (Bishop & Nasrabadi, 2006). We calculate the PCA using all but one “left-out” moonquake waveform. We project the left-out waveform onto each of the principal components to obtain an unbiased coefficient  $m'_{kj}$  for component  $j$  and moonquake  $k$ :

$$m'_{kj} = \text{Gres}_j(t)u_k(t). \quad (2)$$

Here,  $u_k$  is the waveform of the excluded moonquake, and  $\text{Gres}_j$  is the  $j$ th principal component, calculated using the remaining moonquakes. We repeat this process, excluding each available moonquake  $k$  in turn, so that we have a set of unbiased coefficients  $m'_{kj}$  for each moonquake.

We use a bootstrap approach to estimate the uncertainty on the coefficients  $m'_{kj}$ . We again exclude event  $k$  and recompute the principal components, but instead of using all remaining moonquakes in the PCA calculation, we randomly choose from the remaining moonquakes with replacement. With this new subset of moonquakes, we recompute the principal components  $\text{Gres}_j$  and the projected coefficients  $m'_{kj}$  25 times for each event. We also test with 500 bootstraps, which gives similar results (Figure S31 in Supporting Information S1).

The colored circles in Figures 5b–5d show these 25 projected coefficients  $m'_{kj}$  for each of the station S12 MHN moonquakes. The coefficient for the first principal component  $m'_{k1}$  is plotted on the  $x$ -axis. The coefficients of the second ( $m'_{k2}$ ), third ( $m'_{k3}$ ), and twentieth ( $m'_{k20}$ ) principal components are plotted on the  $y$  axis of panels b, c, and d, respectively. Each event  $k$  is plotted in a different color.

Figure 5a summarizes the distribution of the coefficients of the first principal component  $m'_{k1}$  for all moonquakes from the peaked mode S12 data. The distribution of the coefficients is bimodal, with clusters around  $\pm 12$ . Note that a single event can have both a positive and negative  $m'$  because the signs of  $G_j$  and  $m'_{kj}$  can trade-off; in bootstrapping,  $G_j$  can flip and be compensated by a flip in the sign of  $m'_{kj}$ . The nonzero average amplitude of the coefficients, along with the gap around zero, implies that there is a large  $m'_{k1}$  common to all moonquakes. The first principal component thus seems to represent a real Green's function.



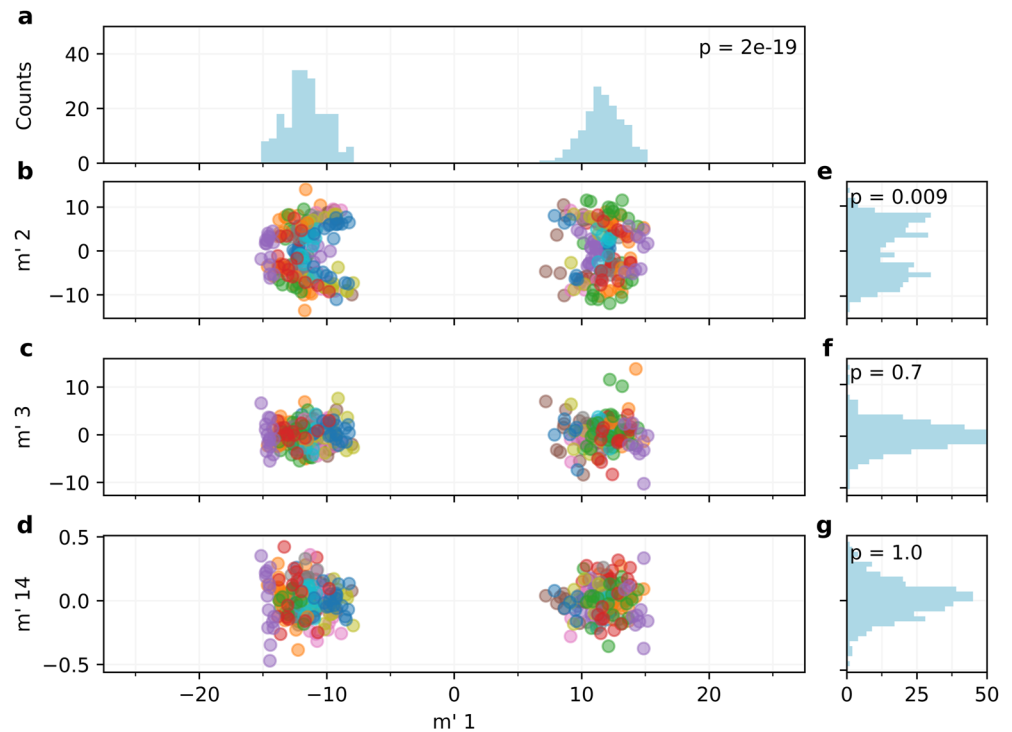


**Figure 5.** Unbiased coefficients of the principal components, from the S12 MHN data in the peaked operational mode. In panels b–d, the coefficient for the first principal component  $m'_{k1}$  is plotted on the x-axis. The coefficients of the second ( $m'_{k2}$ ), third ( $m'_{k3}$ ), and last principal components are plotted on the y axis of panels b, c, and d, respectively. Each event is plotted in a different color. Panels a, e, f, and g summarize the distribution of coefficients for each of the principal components. The text in the top of Panels a, e, f, and g is the probability ( $p$ -value) that each distribution is the same as the distribution of the coefficients derived from noise. Only the first two components differ from noise.

Panel e summarizes the distribution of the coefficients of the second principal component,  $m'_{k2}$ . The bimodal distribution and nonzero average amplitude of the coefficients that imply the second principal component also represents a real Green's function.

Panel f and g summarize the distribution of coefficients for the third and last components. These distributions have only a single peak, and the average values of the distributions are near zero. The near-zero values suggest that although the third component appears moonquake like in Figure 4, there is little moonquake signal in the third and later principal components; it mostly accommodates noise that varies from event to event.

We may more quantitatively compare the coefficient distributions with a Kolmogorov-Smirnov test, a general nonparametric method used to compare two distributions. We assume that the last principal component accommodates only noise, and take its coefficient distribution, plotted in panel g, as representative of the coefficients derived from noise. The distribution of coefficients for the first and second principal components differ from the distribution derived from noise with probabilities of near 100% and 99.1%, respectively (calculated from the Kolmogorov–Smirnov  $p$ -values, which are 1 minus the probability, are  $2e-9$  and 0.009, as shown in the top panel of Figure 5). These coefficients likely accommodate moonquake signals. In this analysis of the peaked mode S12 data, the third component's coefficients differ from the noise with a probability of only 30%. Later components' coefficients are also similar to the distribution of noise.

We obtain similar results when we analyze the distribution of coefficients for all other stations, components, and instrument modes. For example, Figure S16 in Supporting Information S1 summarizes the distribution of coefficients for the station 12 peaked mode MHE waveforms. The distributions of coefficients for the first and second principal components are again bimodal, and the average distribution amplitude is nonzero. The distributions differ from noise with probability near 100% and 99%, respectively. The distribution of coefficients in the third and later principal components have only a single peak at zero and are similar to the distribution of coefficients derived from noise.

Similar although slightly less well-resolved distributions are obtained from flat mode data at station S12 (Figures S17 and S18 in Supporting Information S1). For both the MHN and MHE records, the distributions of coefficients for the first principal components are bimodal, and both differ from noise with probabilities near 100%. The distributions of the second principal components are not bimodal, but they are uniform rather than Gaussian. The distributions still differ from the noise distributions with a probability of 92% and 99% for the MHN and MHE records. The third principal component also differs from noise with a probability of 99%, but it has a large peak at zero. Later components are similar to noise.

Similar results are obtained from station S16, as illustrated in Figures S19–S22 in Supporting Information S1. The distributions from all stations and channels imply that two principal components have a large  $m'_{kj}$  common to multiple moonquakes and represent real Green's functions of slip directions.

## 5.2. Analyzing the Similarity of the Principal Component Vectors ( $G$ )

In the bootstrapping described above, we re-estimated the principal components  $G_j$  and coefficients  $m'_j$  for various subsets of the data, and we analyzed the coefficients  $m'_j$ . In this section, we examine the variation among the estimated principal component vectors  $G_j$ .

We expect little variation in the estimates of a given principal component  $G_j$  if that component recovers a real moonquake signal common to multiple moonquake waveforms. But we expect large variation in bootstrapped estimates of a principal component  $G_j$  if that principal component recovers noise, which varies between waveforms.

We examine the similarity of the bootstrapped principal components using a modified version of the algorithm ICASAR. This algorithm was originally designed to separate ground deformation and atmospheric signals in time series of interferograms using independent component analysis (Gaddes et al., 2019), but we use it to analyze the similarity of our bootstrapped principal component estimates. The similarity between two principal component estimates is quantified as the absolute value of their cross-correlations.

The ICASAR algorithm clusters the bootstrapped principal components according to these cross-correlation values. It uses a hierarchical clustering algorithm (HBDSCAN) to identify similar principal component estimates (Gaddes et al., 2019; McInnes et al., 2017). We assess the quality of clusters using the cluster quality factor  $I_q$ : the difference between the mean intracluster similarity (1 for a perfect cluster) and the mean similarity between members of the cluster and all other component estimates (0 for a perfect cluster).

We would now like to visualize the similarities between the principal component estimates but without plotting the numerous cross-correlations calculated between pairs of events. To do so, we use a visualization technique called the t-distributed stochastic neighbor embedding algorithm. t-distributed stochastic neighbor embedding (t-sne) is an unsupervised, nonlinear technique for visualizing high-dimensional data in a smaller number of dimensions.

We consider the bootstrapped principal components to be a set of points in high dimensional space where the distance between pairs of events is represented by the cross-correlation. The t-sne algorithm then looks for a low-dimensional space where the distances between the points are as similar as possible to those measured by cross-correlation in the high dimensional space. Here, we look for a two dimensional space for easy visualization on paper.

The t-sne visualization in Figure 6 shows the similarity between the recovered principal components in a 2-dimensional space. The values on the  $x$  and  $y$  axis are nonlinear combinations of the cross-correlations; there is one point per bootstrapped principal component. However, it is not the  $x$ - and  $y$ -values that we aim to interpret with this visualization as they are somewhat arbitrary. Only the distance between points—the clustering—is important. With the t-sne visualization, each bootstrapped principal component is given a location so that similar principal components plot close together and dissimilar principal components are separated.

Figure 6 shows the clusters determined using principal components of waveforms recorded at station S12 MHN in peaked mode, visualized using the t-sne algorithm. Only projections from the first four principal components are shown. Points in Figure 6 are colored by the clusters identified by the HBDSCAN algorithm. The principal components estimates in the blue cluster are similar; they have an  $I_q$  of 0.87. The estimates in the orange cluster

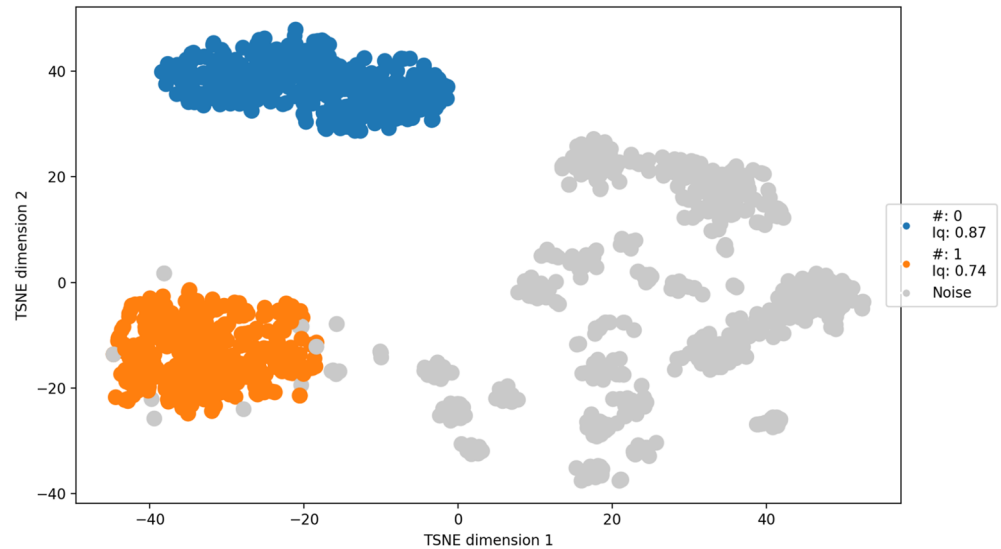


**Figure 6.** Clustering results of bootstrapped principal component vectors  $\mathbf{G}$ , obtained for S12 MHN in peaked operational mode. One point is plotted for each bootstrapped estimate of a principal component, but only the first four principal components are plotted. The location of each point is determined by the t-sne algorithm, preserving the similarity of components from the higher dimensional space (Gaddes et al., 2019; Maaten & Hinton, 2008). The color of each point is determined by the HBDSCAN clustering algorithm (Gaddes et al., 2019; McInnes et al., 2017). Two clusters are shown, in blue and orange. Gray points represent component estimates that are not assigned to a cluster.

have a slightly lower similarity;  $I_q = 0.74$ . Points colored gray represent principal component estimates that are not similar enough to other estimates to form a cluster.

The two clusters identified by the HBDSCAN algorithm and shown visually in Figure 6 suggest that two principal components contain signal common to multiple moonquakes and that these signals are repeatedly recovered in bootstrapping. We obtain similar clusters if we adjust the clustering parameters: if we perturb the minimum cluster size or the distance required to define a “neighbor.” Similar clusters are obtained from other stations, components, and instrument modes (Figures S23–S29 in Supporting Information S1).

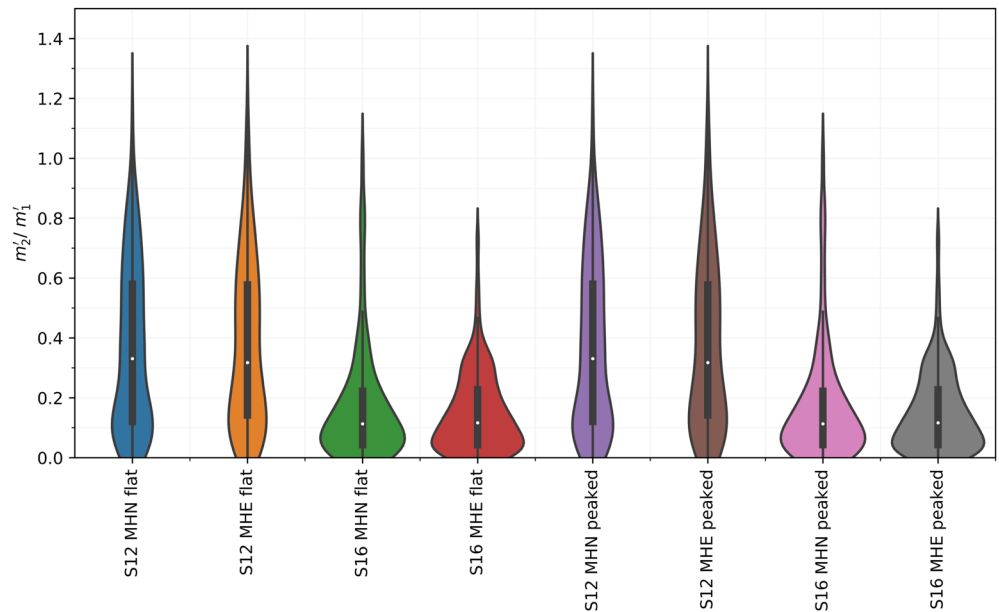
### 5.3. Partitioning of Slip Between Directions

Our analysis in Sections 5.1 and 5.2 implies that two of the recovered principal components contain signal common to many moonquakes, while the others are just noise. We now interpret these two directions as real Green's functions of slip. Since there are two real Green's functions, the moonquakes in the A01 nest slip in a combination of two slip directions. However, we cannot tell in which directions the vectors of the slip directions point, only that there are two.

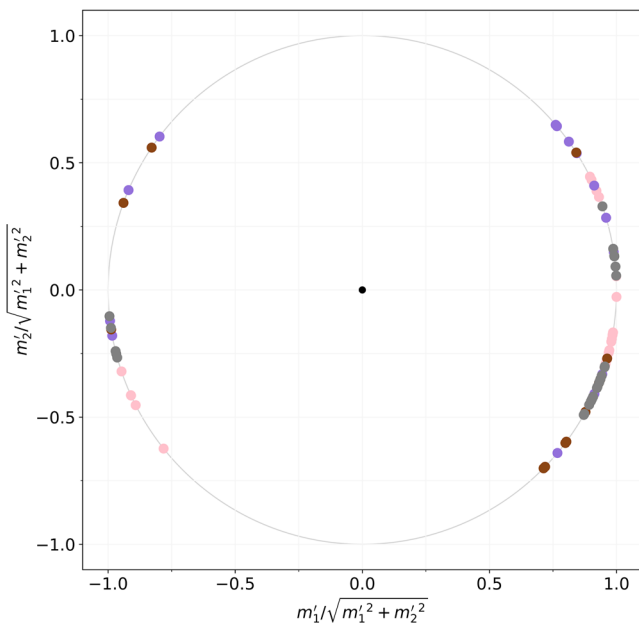
We can now analyze the magnitude of slip in each direction, as we can now interpret the first two coefficients  $m'$  not just as coefficients of principal components but as slip coefficients. Each  $m'_{jk}$  is proportional to the amount of moment in each direction for moonquake  $k$ .

Figure 7 shows distributions of the  $|m'_{1k}/m'_{2k}|$  ratios: the ratio of the moment the second slip direction to the moment in the first slip direction. These distributions are also shown plotted on log axis in Figure S30 in Supporting Information S1. The colored area shows the probability density of the ratio obtained at each station and component, and the white dots mark the median ratio. All distributions are consistent with significant slip in the second direction; distributions have peaks above, not at zero, and the median ratios range from 0.11 to 0.33, with a median at all stations of 0.21.

Finally, we can examine how the slip coefficients vary from moonquake to moonquake. Figure 8 shows the normalized  $m'_{kj}/\sqrt{m'^2_{k1} + m'^2_{k2}}$  values for peaked mode MHN and MHE records at stations S12 and S16. Note that PCA only identifies slip directions that produce different Green's functions, so although the axes in eight are plotted as orthogonal, this is not necessarily the true direction that the different slip vectors would point.



**Figure 7.** Slip coefficient ratio  $m'_{k2}/m'_{k1}$  for each station and channel. The white dot marks the median bootstrapped ratio at each station, the black bar delimits the interquartile range, and the thin black line delimits  $1.5 \times$  the interquartile range. The colored areas illustrate the probability density of the ratio at each station. All distributions have peaks above zero, and the median  $m'_{k2}/m'_{k1}$  ratios range from 0.11 to 0.33.



**Figure 8.** Normalized unbiased slip coefficients for the first and second Green's functions, for moonquakes recorded at both stations, and components in the peaked instrument mode. A vector from each point to the origin would give the slip direction. Negative coefficients in the first slip direction correspond to reversed polarity moonquakes, which slip roughly in the opposite direction of most events. Note, however, that moonquakes appear to slip in a range of direction within the  $m_1$ – $m_2$  plane. The colors correspond to the station and channel considered, as used in Figure 7 (purple: S12 MHN peaked; brown: S12 MHE peaked; pink: S16 MHN peaked; and gray: S16 MHE peaked).

We can nevertheless interpret several features of the varying slip coefficients. First, Figure 8 shows both positive and negative coefficients in the first slip direction. The negative coefficients correspond to moonquakes that slip in the opposite direction of most events; they create the reversed polarity waveforms. Second, and perhaps more interesting, the slip directions do not appear clustered; there is a variable amount of slip in the second direction. Moonquakes appear to slip in a range of directions within a 2-D plane, not in two particular directions.

## 6. Validation

Our analysis implies that two principal components are required to accommodate signal common to many moonquakes in the A01 nest such that these moonquakes slip in two directions. However, some errors have the potential to create artificial principal components. So here, we check that the second significant principal component is a physical feature of the moonquakes and not a result of poor waveform alignment (Section 6.1) or scattered seismic waves (Section 6.2).

### 6.1. Potential Influence of Waveform Alignment

We first check that we have not obtained two principal components because the moonquake waveforms are poorly aligned. We verify that the second principal component is not a time-shifted version of the first component. Then, we examine how the number of significant principal components changes if we add errors in the waveform alignment: if we randomly shift each waveform by a random value drawn from a uniform distribution.

Figure 9 shows the percentage of the variance accommodated by the principal components as we increase the maximum random shift from 0 to 1 s.

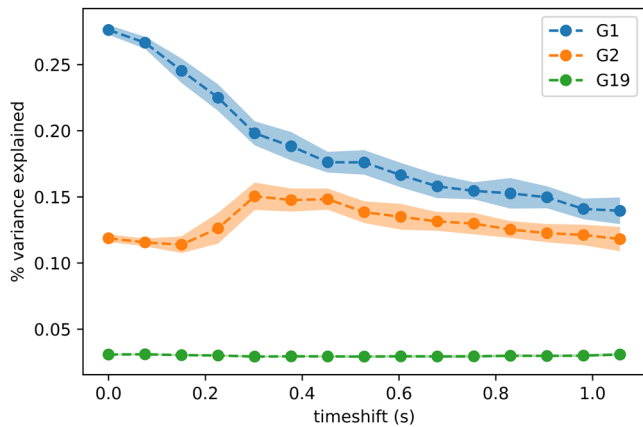


**Figure 9.** Testing the influence of inaccurate waveform alignment. We apply random time-shifts with magnitude up to 1.1s (x-axis) and determine the percentage of the data variance explained by the first (blue), second (orange), and nineteenth (green) principal components.

For shifts up to  $\sim 0.17$  s, energy in the first principal component decreases as the alignment worsens, but that energy is distributed over a number of the later components; the energy in the second principal component does not increase significantly. Bootstrapping analysis of the alignment suggests that the cross-correlation and fine-tuning of the time-shift using PCA allows an accuracy of 0.14 s (2 samples). It thus seems unlikely that the significant energy we observe in the second principal component results from poor waveform alignment.

## 6.2. Potential Influence of Scattering

Next, we assess whether the second slip direction could result from scattering. Moonquakes in the A01 may be in slightly different locations, up to a few km of each other (Nakamura, 2003), and their seismic waves may follow slightly different paths through the Moon, especially in the near-surface scattering layer. The different paths could lead to different recorded seismograms, especially later in the coda, when the seismic waves have been more scattered.

To look for scattering, we apply the PCA to 30-s windows throughout the seismogram, from the direct S wave arrival onward into the coda, as illustrated in Figure 10a. Figure 10b shows the variance explained by the first, second, and last principal components in each of the windows. The different operational modes, components, and stations also give similar results. The variance in the second component does not significantly increase later in the coda, suggesting that scattering later in the coda does not create the significant signal we observe in the second principal component.

## 7. Discussion

In this study, we have used a PCA approach to separate the signal in deep moonquake waveforms into principal components common to multiple moonquakes. We find that two principal components are required to reconstruct the data. These components likely reflect the signals created by slip in two different directions.

### 7.1. Explaining Reversed Polarity Moonquakes

We were motivated to examine moonquake slip directions because some moonquakes have reversed polarity waveforms; these moonquakes appear to slip “backwards.” We sought to determine whether this reversal arises because of a spatially varying tectonic stress, where stress changes direction on either side of a plug (Figure 1b),

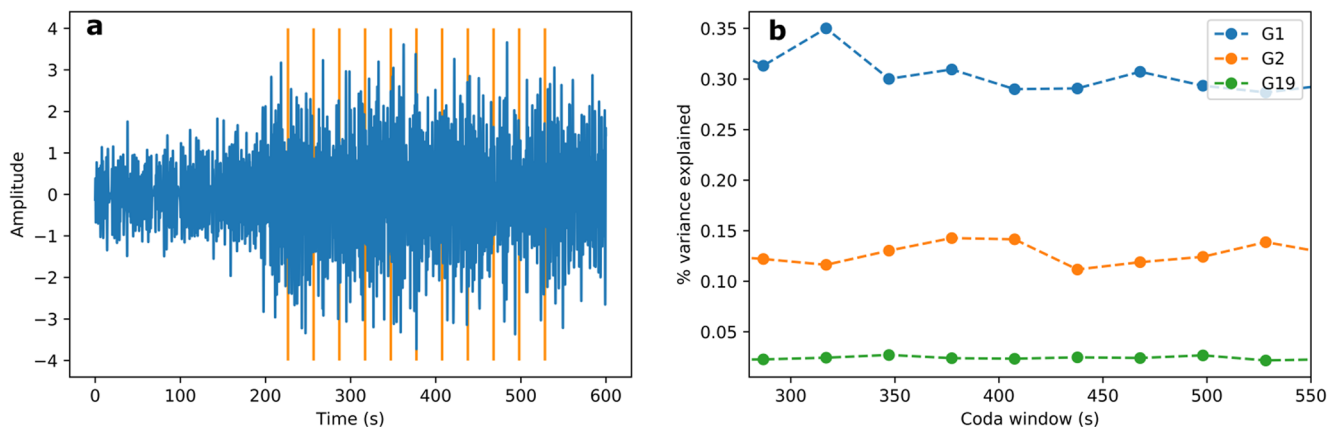


**Figure 10.** (a) A single moonquake waveform, observed at station S12 in flat mode, divided (orange lines) into 30s windows throughout the coda, starting after the high-amplitude S wave arrival. (b) Percentage variance accommodated by the first, second and last components in each time window. The variance percentages remain roughly constant as we move from the direct arrival into the more scattered coda. Scattering thus does not appear to explain the significant signal in the second component.



or whether the reversal arises because the tectonic stress is small, and a tidal stress drives moonquakes and changes direction through time (Figure 1c). To distinguish between these models, we note that the tectonically driven plug model implies only one slip direction: forwards or backwards, while the tidal stress model could allow two slip directions: any combination of forwards, backwards, left, or right. Our observation of two slip directions is more consistent with the tidal model of reversed polarity waveforms.

In principle, however, the plug model could also allow two slip directions. If the two sides of the plug are not parallel, we might see one slip direction (A) on one side of the plug and another direction (B) on the other side. In this case though, the two slip directions would be fixed. Slip might occur in direction A and in direction B but not in any direction along the plane that contains directions A and B. For such a scenario, we could expect the estimated slip coefficient vectors, ( $m_1$ ,  $m_2$ ), as decomposed using PCA, to cluster around two directions, representing slip directions A and B on either side of the plug. We do not observe that clustering.

Instead, we see variation in the first and second slip coefficients (Figure 8). That 2-D variation is more consistent with the tidal model, which allows the slip direction to move along the fault plane as the tidal stress changes.

The variation in the slip direction we observe is also consistent with P/S amplitude variations (Nakamura, 1978) and changes in the slip direction determined from S wave polarities (Koyama & Nakamura, 1980), all of which suggest slip occurs on a fixed fault plane, but the direction of slip can vary with time. Similarly, when resolving the tangential tidal stress and stress rates onto candidate fault planes, Weber et al. (2009) did not find a suitable fault plane for the A01 nest; as they assumed a fixed slip direction in their failure criterion, the lack of a suitable fault plane may also support a variation in the slip direction in the A01 nest.

The two slip directions we identify thus suggest that an oscillating tidal stress drives deep moonquakes in the A01 nest and that this tidal stress changes the local stress direction through time.

## 7.2. Implications of a Small Tectonic Stress

If tidal loading changes the direction of stress in the moonquake region through time, the tidal stresses must be larger than the local tectonic stress. We thus have a new constraint on the magnitude of the tectonic stress at depth; it must be less than the maximum modeled tidal stress of  $\sim 0.1$  MPa (Minshull & Goulety, 1988; Toksöz et al., 1977; Weber et al., 2009).

### 7.2.1. Excluding a Ductile Mechanism for Moonquakes?

We may use this cap on the tectonic stress to help constrain the enigmatic mechanism of deep moonquakes under high pressures and temperatures. Some models have suggested that moonquake slip is driven by a viscous thermal runaway (Thielmann et al., 2015). As the fault slips, the temperature increases, grains reduce in size, and melting can occur, localizing and accelerating the slip on the fault. The runaway process allows ductile failure on seismic timescales. However, large initial shear stresses ( $\sim 100$  MPa at high strain rates (Thielmann et al., 2015)) are required to initialize localization, and those stresses are not compatible with our 0.1 MPa upper bound on the tidal and tectonic stress in the A01 moonquake region. This allows us to rule out this mechanism for deep moonquakes.

A variety of models remain to explain the rapid failure that creates moonquakes at high pressure and temperature, though all the models remain poorly tested. One model suggests that high pore fluid pressure could reduce the effective stress on faults at depth and enable deep moonquake faults to slip. The lunar interior is wetter than previously thought (Evans et al., 2014). However, it remains unclear whether there is enough water in the right places to account for the generation of deep moonquakes.

Alternatively, deep moonquakes could be caused by a volume change associated with a mineralogical phase change leading to faulting as proposed for deep-focus ( $>400$  km) earthquakes. A volumetric component of deep moonquake failure was suggested as a possibility by Weber et al. (2009) when no plane of failure could be correlated with the peak tidal stress at the time of moonquake occurrence. However, this model is only suitable if (a) there is an appropriate phase transition in the lunar interior (pressures on the Moon are too low for the olivine-spinel transformation invoked in the Earth for deep-focus seismicity) and (b) this phase change could repeatedly happen in the same location. However, current models of the lunar interior do not identify a suitable phase change (Garcia et al., 2011), making this mechanism unlikely.

### 7.2.2. Lunar Interior

In addition to improving our understanding of the mechanism of deep moonquakes, our moonquake-derived stress bounds, which imply that the local tectonic stress is smaller than the tidal stress, also provide constraints on thermal and dynamic models of the lunar interior. This stress bound implies that any stress from thermal contraction must be less than 0.1 MPa, consistent with previous estimates (Solomon & Chaiken, 1976). We can also place an upper bound on any remaining convection. If we assume a Newtonian viscosity of  $10^{21}$  Pa s (e.g., Li et al., 2019), a long term stress smaller than 0.1 MPa implies a local strain rate smaller than  $10^{-16}$  s $^{-1}$ . Future research may find other uses for our moonquake-derived stress bounds. For example, the bounds might be used to provide constraints on stress concentrations around local heterogeneity within the lunar interior (Qin et al., 2012; Sakamaki et al., 2010; Steinberger et al., 2015; Zhao et al., 2012).

### 7.3. Further Application to Moonquakes and Earthquakes

The methodology developed in this study may also be relevant for future work. We have applied the PCA methodology only to the A01 nest, but this technique could let us examine more moonquakes, as recorded in the Apollo data or in data collected by the new broadband seismometer on the Farside Seismic Suite package, expected to land on the far side of the Moon in 2024 or 2025.

The PCA method appears necessary on the Moon, but it could also be useful for events on Earth, particularly in situations where there is no clear first arrival or where network coverage is sparse.

## 8. Conclusion

In this work, we sought both to understand the origin of moonquakes that slip “backwards” and to constrain the relative magnitudes of tidal and tectonic stresses deep in the lunar interior. Our observation of two slip directions implies that moonquakes’ reversed polarity waveforms result from an oscillating tidal stress, which encourages moonquakes to slip forwards, backwards, left, or right depending on the phase of the tide. To explain these varying slip directions, the tidal stresses, which have a magnitude around 0.1 MPa (Minshall & Goulet, 1988; Toksöz et al., 1977; Weber et al., 2009), must be larger than the local tectonic stress. Our observations thus imply that the tectonic stress near the A01 nest, at 900 km depth, is less than 0.1 MPa. That small tectonic stress may be employed in future modeling of the lunar interior. Further, the small stress implies that viscous thermal runaway, which requires a large stress for initiation (Thielmann et al., 2015), is unlikely to explain the existence of deep moonquakes.

## Data Availability Statement

A jupyter notebook containing a simple tutorial on using PCA for moonquake waveforms and derived data is available at <https://doi.org/10.5281/zenodo.7217786> (Turner, 2022).

## References

- Araki, H. (2001). Focal processes of deep moonquakes. *Journal of the Geodetic Society of Japan*, 47(1), 508–513.
- Bishop, C. M., & Nasrabadi, N. M. (2006). *Pattern recognition and machine learning* (Vol. 4). Springer.
- Brantut, N., Sulem, J., & Schubnel, A. (2011). Effect of dehydration reactions on earthquake nucleation: Stable sliding, slow transients, and unstable slip. *Journal of Geophysical Research*, 116(B5), B05304. <https://doi.org/10.1029/2010jb007876>
- Bulow, R., Johnson, C., & Shearer, P. (2005). New events discovered in the Apollo lunar seismic data. *Journal of Geophysical Research*, 110(E10), E10003. <https://doi.org/10.1029/2005je002414>
- Burnley, P. C., Green, H. W., & Prior, D. J. (1991). Faulting associated with the olivine to spinel transformation in Mg<sub>2</sub>GeO<sub>4</sub> and its implications for deep-focus earthquakes. *Journal of Geophysical Research*, 96(B1), 425–443. <https://doi.org/10.1029/90jb01937>
- Cheng, C. H., & Toksöz, M. N. (1978). Tidal stresses in the moon. *Journal of Geophysical Research*, 83(B2), 845–853. <https://doi.org/10.1029/jb083ib02p00845>
- Davies, J. H. (1999). The role of hydraulic fractures and intermediate depth earthquakes in subduction zone magmatism. *Nature*, 398(6723), 142–145. <https://doi.org/10.1038/18202>
- Dobson, D., Meredith, P., & Boon, S. (2002). Microseismicity associated with antigorite dehydration: Laboratory simulation of deep-focus earthquakes. In *EGS general assembly conference abstracts* (p. 3985).
- Evans, A., Zuber, M., Weiss, B., & Tikoo, S. (2014). A wet, heterogeneous lunar interior: Lower mantle and core dynamo evolution. *Journal of Geophysical Research: Planets*, 119(5), 1061–1077. <https://doi.org/10.1002/2013je004494>
- Frohlich, C., & Nakamura, Y. (2009). The physical mechanisms of deep moonquakes and intermediate-depth earthquakes: How similar and how different? *Physics of the Earth and Planetary Interiors*, 173(3–4), 365–374. <https://doi.org/10.1016/j.pepi.2009.02.004>

## Acknowledgments

The authors thank the editor Laurent Montési and reviewers Taichi Kawamura and an anonymous reviewer for their valuable reviews, which helped improve the manuscript. We gratefully acknowledge the availability of the long period Apollo seismic data from the Institut de Physique du Globe de Paris (IPGP) data center (<http://datacenter.ipgp.fr/>). The implementation of the ICASAR algorithm for clustering and visualization is from Gaddes et al. (2019). Figures were prepared in Matplotlib (Hunter, 2007). We would like to thank Ceri Nunn and Taichi Kawamura for their useful insights on the Apollo seismic data. AT was supported by STFC studentship ST/S505626/1.

- Gaddes, M., Hooper, A., & Bagnardi, M. (2019). Using machine learning to automatically detect volcanic unrest in a time series of interferograms. *Journal of Geophysical Research: Solid Earth*, 124(11), 12304–12322. <https://doi.org/10.1029/2019jb017519>
- Gagnepain-Beyneix, J., Lognonné, P., Chenet, H., Lombardi, D., & Spohn, T. (2006). A seismic model of the lunar mantle and constraints on temperature and mineralogy. *Physics of the Earth and Planetary Interiors*, 159(3–4), 140–166. <https://doi.org/10.1016/j.pepi.2006.05.009>
- Garcia, R. F., Gagnepain-Beyneix, J., Chevrot, S., & Lognonné, P. (2011). Very preliminary reference moon model. *Physics of the Earth and Planetary Interiors*, 188(1–2), 96–113. <https://doi.org/10.1016/j.pepi.2011.06.015>
- Garcia, R. F., Khan, A., Drilleau, M., Margerin, L., Kawamura, T., Sun, D., et al. (2019). Lunar seismology: An update on interior structure models. *Space Science Reviews*, 215(8), 1–47. <https://doi.org/10.1007/s11214-019-0613-y>
- Green, H., & Burnley, P. (1989). A new self-organizing mechanism for deep-focus earthquakes. *Nature*, 341(6244), 733–737. <https://doi.org/10.1038/341733a0>
- Hacker, B. R., Peacock, S. M., Abers, G. A., & Holloway, S. D. (2003). Subduction factory 2. Are intermediate-depth earthquakes in subducting slabs linked to metamorphic dehydration reactions? *Journal of Geophysical Research*, 108(B1), 2030. <https://doi.org/10.1029/2001jb001129>
- Hardebeck, J. L., & Shearer, P. M. (2002). A new method for determining first-motion focal mechanisms. *Bulletin of the Seismological Society of America*, 92(6), 2264–2276. <https://doi.org/10.1785/0120010200>
- Hunter, J. D. (2007). Matplotlib: A 2D graphics environment. *Computing in Science & Engineering*, 9(03), 90–95. <https://doi.org/10.1109/mcse.2007.55>
- John, T., Medvedev, S., Rüpk, L. H., Andersen, T. B., Podladchikov, Y. Y., & Austrheim, H. (2009). Generation of intermediate-depth earthquakes by self-localizing thermal runaway. *Nature Geoscience*, 2(2), 137–140. <https://doi.org/10.1038/ngeo419>
- Karato, S.-I., Riedel, M. R., & Yuen, D. A. (2001). Rheological structure and deformation of subducted slabs in the mantle transition zone: Implications for mantle circulation and deep earthquakes. *Physics of the Earth and Planetary Interiors*, 127(1–4), 83–108. [https://doi.org/10.1016/s0031-9201\(01\)00223-0](https://doi.org/10.1016/s0031-9201(01)00223-0)
- Kawamura, T., Lognonné, P., Nishikawa, Y., & Tanaka, S. (2017). Evaluation of deep moonquake source parameters: Implication for fault characteristics and thermal state. *Journal of Geophysical Research: Planets*, 122(7), 1487–1504. <https://doi.org/10.1002/2016JE005147>
- Kelemen, P. B., & Hirth, G. (2007). A periodic shear-heating mechanism for intermediate-depth earthquakes in the mantle. *Nature*, 446(7137), 787–790. <https://doi.org/10.1038/nature05717>
- Khan, A., Connolly, J. A., Pommier, A., & Noir, J. (2014). Geophysical evidence for melt in the deep lunar interior and implications for lunar evolution. *Journal of Geophysical Research: Planets*, 119(10), 2197–2221. <https://doi.org/10.1002/2014je004661>
- Kirby, S. H. (1987). Localized polymorphic phase transformations in high-pressure faults and applications to the physical mechanism of deep earthquakes. *Journal of Geophysical Research*, 92(B13), 13789–13800. <https://doi.org/10.1029/jb092ib13p13789>
- Kirby, S. H., Stein, S., Okal, E. A., & Rubie, D. C. (1996). Metastable mantle phase transformations and deep earthquakes in subducting oceanic lithosphere. *Reviews of Geophysics*, 34(2), 261–306. <https://doi.org/10.1029/96rg01050>
- Koyama, J., & Nakamura, Y. (1980). Focal mechanism of deep moonquakes. In *Lunar and planetary science conference proceedings*, (Vol. 11, pp. 1855–1865).
- Lammlin, D. R. (1977). Lunar seismicity and tectonics. *Physics of the Earth and Planetary Interiors*, 14(3), 224–273. [https://doi.org/10.1016/0031-9201\(77\)90175-3](https://doi.org/10.1016/0031-9201(77)90175-3)
- Li, H., Zhang, N., Liang, Y., Wu, B., Dygert, N. J., Huang, J., & Parmentier, E. (2019). Lunar cumulate mantle overturn: A model constrained by ilmenite rheology. *Journal of Geophysical Research: Planets*, 124(5), 1357–1378. <https://doi.org/10.1029/2018je005905>
- Maaten, L. V. D., & Hinton, G. (2008). Visualizing data using t-SNE. *Journal of Machine Learning Research*, 9, 2579–2605.
- McInnes, L., Healy, J., & Astels, S. (2017). hdbscan: Hierarchical density based clustering. *Journal of Open Source Software*, 2(11), 205. <https://doi.org/10.21105/joss.00205>
- Meade, C., & Jeanloz, R. (1991). Deep-focus earthquakes and recycling of water into the Earth's mantle. *Science*, 252(5002), 68–72. <https://doi.org/10.1126/science.252.5002.68>
- Minshall, T., & Goulet, N. (1988). The influence of tidal stresses on deep moonquake activity. *Physics of the Earth and Planetary Interiors*, 52(1–2), 41–55. [https://doi.org/10.1016/0031-9201\(88\)90056-8](https://doi.org/10.1016/0031-9201(88)90056-8)
- Nakamura, Y. (1978). A1 moonquakes-source distribution and mechanism. In *Lunar and planetary science conference proceedings*, (Vol. 9, pp. 3589–3607).
- Nakamura, Y. (2003). New identification of deep moonquakes in the Apollo lunar seismic data. *Physics of the Earth and Planetary Interiors*, 139(3–4), 197–205. <https://doi.org/10.1016/j.pepi.2003.07.017>
- Nakamura, Y. (2005). Spatial extent of a deep moonquake nest—a preliminary report of reexamination. In *36th annual lunar and planetary science conference* (p. 1168).
- Nunn, C., Garcia, R. F., Nakamura, Y., Marusiak, A. G., Kawamura, T., Sun, D., et al. (2020). Lunar seismology: A data and instrumentation review. *Space Science Reviews*, 216(5), 1–39. <https://doi.org/10.1007/s11214-020-00709-3>
- Nunn, C., Nakamura, Y., & Igel, H. (2017). Apollo passive seismic experiments: Lunar data in seed format. In *AGU fall meeting abstracts* (pp. P41D–P2860).
- Nunn, C., Weber, R. C., & Panning, M. (2020). Improving the accessibility of the Apollo seismic data: Archiving at iris and the PDS. In *Lunar and planetary science conference* (p. 2269).
- Ocaña, E., Stich, D., Carmona, E., Vidal, F., Bretón, M., Navarro, M., & García-Jerez, A. (2008). Spatial analysis of the La Paca, SE Spain, 2005 seismic series through the relative location of multiplets and principal component analysis. *Physics of the Earth and Planetary Interiors*, 166(3–4), 117–127. <https://doi.org/10.1016/j.pepi.2007.12.005>
- Ogawa, M. (1987). Shear instability in a viscoelastic material as the cause of deep focus earthquakes. *Journal of Geophysical Research*, 92(B13), 13801–13810. <https://doi.org/10.1029/jb092ib13p13801>
- Proctor, B., & Hirth, G. (2015). Role of pore fluid pressure on transient strength changes and fabric development during serpentine dehydration at mantle conditions: Implications for subduction-zone seismicity. *Earth and Planetary Science Letters*, 421, 1–12. <https://doi.org/10.1016/j.epsl.2015.03.040>
- Qin, C., Muirhead, A. C., & Zhong, S. (2012). Correlation of deep moonquakes and mare basalts: Implications for lunar mantle structure and evolution. *Icarus*, 220(1), 100–105. <https://doi.org/10.1016/j.icarus.2012.04.023>
- Sakamaki, T., Ohtani, E., Urakawa, S., Suzuki, A., Katayama, Y., & Zhao, D. (2010). Density of high-ti basalt magma at high pressure and origin of heterogeneities in the lunar mantle. *Earth and Planetary Science Letters*, 299(3–4), 285–289. <https://doi.org/10.1016/j.epsl.2010.09.007>
- Schubnel, A., Brunet, F., Hilaret, N., Gasc, J., Wang, Y., & Green, H. W. (2013). Deep-focus earthquake analogs recorded at high pressure and temperature in the laboratory. *Science*, 341(6152), 1377–1380. <https://doi.org/10.1126/science.1240206>
- Solomon, S., & Chaiken, J. (1976). Thermal expansion and thermal stress in the moon and terrestrial planets-clues to early thermal history. In *Lunar and planetary science conference proceedings*, (Vol. 7, pp. 3229–3243).

- Steinberger, B., Zhao, D., & Werner, S. C. (2015). Interior structure of the moon: Constraints from seismic tomography, gravity and topography. *Physics of the Earth and Planetary Interiors*, 245, 26–39. <https://doi.org/10.1016/j.pepi.2015.05.005>
- Thielmann, M. (2018). Grain size assisted thermal runaway as a nucleation mechanism for continental mantle earthquakes: Impact of complex rheologies. *Tectonophysics*, 746, 611–623. <https://doi.org/10.1016/j.tecto.2017.08.038>
- Thielmann, M., Rozel, A., Kaus, B., & Ricard, Y. (2015). Intermediate-depth earthquake generation and shear zone formation caused by grain size reduction and shear heating. *Geology*, 43(9), 791–794. <https://doi.org/10.1130/g36864.1>
- Toksöz, M. N., Goins, N. R., & Cheng, C. (1977). Moonquakes: Mechanisms and relation to tidal stresses. *Science*, 196(4293), 979–981. <https://doi.org/10.1126/science.196.4293.979>
- Turner, A. R. (2022). Deep\_Moonquake\_PCA: Data and code for Stresses in the lunar interior: Insights from slip directions in the A01 deep moonquake nest (Version 1) [Computer software]. Zenodo. <https://doi.org/10.5281/ZENODO.7217786>
- Vasco, D. (1989). Deriving source-time functions using principal component analysis. *Bulletin of the Seismological Society of America*, 79(3), 711–730. <https://doi.org/10.1785/bssa0790030711>
- Vasco, D. (1990). Seismic source representation in orthogonal functions. *Geophysical Journal International*, 102(3), 531–535. <https://doi.org/10.1111/j.1365-246x.1990.tb04579.x>
- Vavryčuk, V., Adamová, P., Doubravová, J., & Jakoubková, H. (2017). Moment tensor inversion based on the principal component analysis of waveforms: Method and application to microearthquakes in west bohemia, Czech Republic. *Seismological Research Letters*, 88(5), 1303–1315. <https://doi.org/10.1785/0220170027>
- Weber, R. C., Bills, B., & Johnson, C. (2009). Constraints on deep moonquake focal mechanisms through analyses of tidal stress. *Journal of Geophysical Research*, 114(E5), E05001. <https://doi.org/10.1029/2008je003286>
- Weber, R. C., Bills, B. G., & Johnson, C. L. (2010). A simple physical model for deep moonquake occurrence times. *Physics of the Earth and Planetary Interiors*, 182(3–4), 152–160. <https://doi.org/10.1016/j.pepi.2010.07.009>
- White, R. S., Drew, J., Martens, H. R., Key, J., Soosalu, H., & Jakobsdóttir, S. S. (2011). Dynamics of dyke intrusion in the mid-crust of Iceland. *Earth and Planetary Science Letters*, 304(3–4), 300–312. <https://doi.org/10.1016/j.epsl.2011.02.038>
- Yang, W., Hauksson, E., & Shearer, P. M. (2012). Computing a large refined catalog of focal mechanisms for southern California (1981–2010): Temporal stability of the style of faulting. *Bulletin of the Seismological Society of America*, 102(3), 1179–1194. <https://doi.org/10.1785/0120110311>
- Zhao, D., Arai, T., Liu, L., & Ohtani, E. (2012). Seismic tomography and geochemical evidence for lunar mantle heterogeneity: Comparing with Earth. *Global and Planetary Change*, 90, 29–36. <https://doi.org/10.1016/j.gloplacha.2012.01.004>